

**Response of OH airglow emissions to the mesospheric gravity waves and its  
comparisons with full wave model simulation at a low latitude Indian station**

**R. N. Ghodpage<sup>1</sup>, M. P. Hickey<sup>2</sup>, A. Taori<sup>3,4</sup>, Devendraa Siingh<sup>5</sup> and P. T. Patil<sup>1</sup>**

[1] {Indian Institute of Geomagnetism, Shivaji University Campus, Kolhapur 416004, India}

[2] {Embry-Riddle Aeronautical University, FL - 32114, USA}

[3] {National Atmospheric Research Laboratory, Pakala Mandal, Gadanki ( A. P.) 517112,  
India}

[4] {now at- National Remote Sensing Center (NRSC), Hyderabad, 500037, India}

[5] {Indian Institute of Tropical Meteorology, Pune-411 008, Maharashtra, India}

**Abstract:**

The quasi-monochromatic gravity wave induced oscillations, monitored using the mesospheric OH airglow emission over Kolhapur (16.8°N and 74.2°E), India during January to April 2010 and January to December 2011, have been characterized using the Krassovsky method. The nocturnal variability reveals prominent wave signatures with periods ranging from 5.2-10.8 hr as the dominant nocturnal wave with embedded short period waves having wave periods 1.5-4.4 hr. The results show that the magnitude of the Krassovsky parameter, viz.,  $|\eta|$  ranged from 2.1 to 10.2 for principal or long nocturnal waves (5.2 to 10.8 hr observed periods), and, from 1.5 to 5.4 for the short waves (1.5 to 4.4 hr observed periods) during the years of 2010 and 2011, respectively. The phase, i.e.,  $\Phi$  values of the Krassovsky parameters exhibited larger variability and varied from  $-8.1^\circ$  to  $-167^\circ$ . The deduced mean vertical wavelengths are found to be approximately  $-60.2 \pm 20$  km and  $-42.8 \pm 35$  km for long and short wave periods for the year 2010. Similarly, for 2011 the mean vertical wavelengths are found to be approximately  $-77.6 \pm 30$  km and  $-59.2 \pm 30$  km for long and short wave periods, respectively, indicating that the observations over Kolhapur were dominated by upward propagating waves. We use a full wave model to simulate the response of OH emission to the wave motion and compare the results with observed values. **Keywords:** OH emissions, Mesospheric gravity wave, Full wave model

## 1. Introduction

The airglow Hydroxyl emissions (OH) have been widely used for studying atmospheric temperature variation in the mesopause region since the pioneering work of Meinel (1950) and its usefulness to derive the rotational temperature (Greet et al., 1998, Bittner et al., 2000). The collision frequency of OH with the neutral atmosphere in the neighborhood of 90 km of altitude should be in an order to  $10^4 \text{ s}^{-1}$  and the life time of the excited Hydroxyl emission is around 3 to 10 msec. (Mies, 1974). This ensures that the excited OH molecules in the rotational energy levels are in a thermal equilibrium with the atmospheric ambient gases (Sivjee & Hamwey, 1987, Takahashi et al., 1998). Thus, it is normally assumed that the rotational state of OH band is in Maxwell-Boltzmann distribution. The radiated light intensity provides a direct measure of OH quantum state distribution in the mesopause. Meriwether (1975) arrived at an expression for the P1(2) and P1 (5) rotational lines of OH (8-3) band by making use of the vibration-rotation transition probabilities of Mies (1974). Therefore using two lines from a single band we can estimate the rotational temperature by the given equation (Mies, 1974):

$$T_{n,m} = \frac{E_{v'}(J'_m) - E_{v'}(J'_n)}{k \ln \left[ \frac{I_n}{I_m} \frac{A(J'_m, v' \rightarrow J''_{m+1}, v'')}{A(J'_n, v' \rightarrow J''_{n+1}, v'')} \frac{2J'_m + 1}{2J'_n + 1} \right]}$$

Where  $T_{n,m}$  is the rotational temperature calculated from two line intensities,  $I_n$  and  $I_m$ , from rotational levels  $J'_n, J'_m$  in the upper vibrational level  $v'$ , to  $J''_{n+1}, J''_{m+1}$  in the lower vibrational level  $v''$ .  $E_v(J)$  is the energy of the level  $(J, v)$ .  $A(J'_n, v' \rightarrow J''_{n+1}, v'')$  is the Einstein coefficient, for the transition from  $J'_n, v'$  to  $J''_{n+1}, v''$ . The intensity ratio between P1 (2) and P1 (5) lines of the OH(8,3) band were used to obtain rotational temperature using the transition probabilities as

given by Mies (1974). Often the observed temporal variations in the mesospheric hydroxyl OH night airglow intensities and rotational temperatures are caused by propagating gravity waves from the lower to the upper atmosphere.

The interaction of these upward propagating waves with the ambient and other waves contribute to the dynamical variability, which in turn is reflected in observed airglow intensity and temperature perturbations (Hines, 1997). Krassovsky (1972) introduced a quantity ‘ $\eta$ ’ to characterize the wave-induced perturbations. This parameter, termed as ‘Krassovsky’s parameter’, is now defined as  $\eta = |\eta| e^{-i\Phi}$ , where  $|\eta|$  indicates the ratio of the amplitude variation between the emission intensity and temperature perturbations normalized to their time averages and  $\Phi$  is the phase difference between the intensity wave and its temperature counterpart (e.g., Walterscheid et al., 1987; Taylor et al., 1991). It should also be mentioned that apart from the pure dynamical processes  $\eta$  can also be affected by various other unknown parameters, such as the variation of local oxygen photochemistry (Hickey et al., 1993) and height variation of the emission layer, which affects emission rates and temperature directly (Liu and Swenson 2003; Vargas et al., 2007). Although this can complicate studies of Krassovsky’s parameter, it offers an opportunity to study the above aspects. Overall, once the physics and chemistry of emissions are well understood, the  $\eta$  values would offer a good tool to study the perturbations caused in a parameter (temperature, brightness/intensity) by measuring one under the assumption that gravity wave induced perturbations are of adiabatic nature.

Utilizing the above, many investigators have carried out observational as well as theoretical studies on the identification and characterization of gravity wave and tidal signatures with wave periodicities ranging from few minutes to several hours (e.g., Walterscheid et al., 1987; Hecht et al., 1987; Hickey 1988a, b; Taylor et al., 1991; Takahashi et al., 1992; Reisin

and Scheer 1996; Taori and Taylor 2006; Guharay et al., 2008; Ghodpage et al., 2012, 2013 ). However, observational studies of the magnitude and phase of  $\eta$  over a range of wave periods for a given location and season are sparse. Some of the notable observations of  $\eta$  for the OH emission have been performed by Viereck and Deehr (1989) in the wave period range of  $\sim 1 - 20$  hr and by Reisin and Scheer (1996) near to the semidiurnal tidal fluctuations.

In the present work, we utilize the mesospheric OH emission intensity and temperature data obtained during January - April 2010 and January - December 2011, when clear and moonless nights allowed observations to exceed 5 hours duration. We deduce the Krassovsky parameters as a function of observed wave period and also infer the vertical wavelengths for the observed mesospheric waves. Further, we compare our estimates with the earlier results reported by various investigators. We also employ a full-wave model to simulate the effects of wave motions on the OH airglow. This model has been used previously to compare observations and theory of airglow fluctuations (e.g., Hickey et al., 1998; Hickey and Yu 2005). Here, the model is used to estimate the values of the amplitudes and phases of Krassovsky's ratio which are compared to those derived from the observations, making the present study unique as such model comparison over India has not been done before.

## **2. Instrumentation and Observations**

The mesospheric OH observations are made using the multispectral photometer from Kolhapur (16.8°N, 74.2°E) (Ghodpage et al., 2013, 2014). We analyze the data from January - April 2010 and January-December 2011 when clear sky conditions prevailed for several nights. For the year 2010, 13 nights out of 45 nights of observation clearly showed wavelike features, while in 2011, 29 from 60 nights of data exhibited wavelike variations.

## 99    **2.1    The multispectral photometer**

100    Regular observations of the night airglow emissions, OI 630.0 nm, OI 557.7nm and OH Meinel  
 101    (731 nm and 740 nm) band have been carried out at the low latitude station Kolhapur. We have  
 102    operated multispectral photometer pointing to the zenith over Kolhapur. The filters have a band  
 103    width of 1 nm and their temperature is controlled by a temperature controller at 24 °C. The  
 104    temperature coefficient of filter is 0.011 nm/ °C. At 24°C the transmission efficiency of filters is  
 105    40 - 70 %. We kept the integration time for each filter 15 seconds which results in repetition time  
 106    of 90 seconds with an accuracy of approximately  $\pm 0.5\%$  for line intensity. The photometer has  
 107    F/2 optics with  $\sim 10^\circ$  full field of view. The stepper motor rotation and sensing of the initial  
 108    position is performed by computer controlled software. As the detector, the EMI9658B  
 109    photomultiplier tube is used. An amplifier (high gain trans-impedance) is used to convert and  
 110    amplify the very weak photomultiplier output current (in the range of nA) into corresponding  
 111    voltage form. In the absence of standard calibration source, we have used relative intensities  
 112    (arbitrary units). In order to study the wave features present in the MLT region, we consider clear  
 113    sky nights having more than 5 hours of continuous OH band data as mentioned in earlier reports  
 114    (e.g., Taori et al., 2005).

115

## 116    **2.2    Full Wave Model**

117    The full-wave model is a linear, steady-state model that solves the linearized Navier-Stokes  
 118    equations on a high resolution vertical grid to describe the vertical propagation of acoustic-  
 119    gravity waves in a windy background atmosphere including molecular viscosity and thermal  
 120    conduction, ion drag, Coriolis force and the eddy diffusion of heat and momentum in the

mesosphere. The model description, including equations, boundary conditions and method of solution has been described elsewhere (Hickey et al., 1997; Walterscheid and Hickey 2001; Schubert et al., 2003). The neutral perturbations are used as input to a linear, steady-state model describing OH airglow fluctuations (Hickey and Yu 2005).

The model solves the equations on a high resolution vertical grid subject to boundary conditions, and allows generally for the propagation in a height varying atmosphere (non-isothermal mean state temperature and height varying mean winds and diffusion). The linearized equations are numerically integrated from the lower to the upper boundary using the tri-diagonal algorithm described by Bruce et al. (1958) and Lindzen and Kuo (1969). The lower boundary is set well below the region of interest and a sponge layer is implemented to avoid effects of wave reflection in the airglow response. In this study the lower boundary (the bottom of the lower sponge layer) is placed at 250 km below  $z = 0$  (i.e., -250 km). The wave forcing is through the addition of heat in the energy equation. The heating is defined by a Gaussian profile with a full-width-at-half-max of 0.125 km. It is centered at an altitude of 10 km. A Rayleigh-Newtonian sponge layer, in addition to natural absorption by viscosity and heat conduction prevents spurious reflection from the upper boundary. At the upper boundary (here 300 km altitude) a radiation condition is imposed using a dispersion equation that includes viscous and thermal dissipation (Hickey and Cole 1987). The mean state is defined using the Mass Spectrometer Incoherent Scatter (MSIS) model (Hedin 1991).

A set of linear perturbation equations for the minor species involved in the OH emission chemistry is solved using the approach described in Hickey (1988). This assumes that these minor species have the same velocity and temperature perturbations as the major gas (which are deduced from the full-wave model). A vertical integration of the volume emission rates through

the vertical extent of the OH layer provides the brightness and brightness-weighted temperature perturbations, from which Krassovsky's ratio is determined. The OH chemistry we use is the same as that used previously (Hickey et al., 1997) and is for the OH (8-3) emission. We also determine the vertical wavelength at the peak of the OH emission layer evaluated from the phase variations of the temperature perturbations determined by the full-wave model.

### 2.3 Space borne measurements

The Sounding of the Atmosphere using Broadband Emission Radiometry (SABER), on-board the Thermosphere Ionosphere Mesosphere Energetic and Dynamics (TIMED) satellite, is a high-precision broadband radiometer which measures limb radiance (orbital inclination at  $74^\circ$ ) of the terrestrial atmosphere in 10 selected spectral bands ranging from 1.27 to 15  $\mu\text{m}$ . In the present study, we note larger values of  $|\eta|$  occur during 2011 compared to 2010 for long/principal waves, which indicates a larger intensity to temperature perturbation ratio over Kolhapur during the passage of the waves during 2011. This could be due to the differences in either the background atmosphere or the dynamical processes. To identify the differences in the OH emission layer in year 2010 and 2011, we scrutinize the OH volume emission rate profile for Kolhapur region obtained from SABER. The selected latitude–longitude grids are  $10^\circ\text{N}$  to  $20^\circ\text{N}$  and  $70^\circ\text{E}$  to  $90^\circ\text{E}$  representing Kolhapur. The criteria for the selection of SABER data are such that: (i) the SABER pass should be during typical observation times (excluding twilight time).

## 3. Results and Discussion



To identify the wave structures in the data, we utilize the perturbation amplitudes normalized to their time averaged values (hereafter referred to as mean values) in the intensity and temperature data to calculate the Krassovsky ratio. To illustrate this, we show a typical example corresponding to the data obtained on 26 - 27 January 2011 in Figure 1. We plot the intensity deviations from their mean values in figure 1(a), while, the temperature deviations from their mean values are plotted in figure 1(b). We note that night airglow intensity variations show a long-period wave with embedded short-period oscillatory features. On this night, the mean airglow intensity is found to be  $\sim 1.83$  arbitrary units and the mean temperature data is  $\sim 195.75$  K. To identify the nocturnal variability plotted together with data as solid red lines are the best-fit cosine model (e.g., Taori et al., 2005) as follows.

$$Y = A \cos \left[ \pi \frac{(X - X_c)}{T} \right] \quad (1)$$

where, A is the amplitude of the fitted wave of half-period T with phase  $X_c$ , and X is the time. The solid red lines in figure 1 show the results of the best-fit cosine model. We observed the presence of  $\sim 8.2 \pm 1.1$  hr and  $8 \pm 1.3$  hr waves with relative amplitudes (normalized to their mean values and converted to corresponding % amplitude)  $\sim 3.6\%$  and  $25.64\%$ , in the nocturnal temperature and intensity variability, respectively. Given the uncertainties involved in the observations, we consider these to be the same waves. Further, we compute the  $|\eta|$  value for this wave to be  $7.12 \pm 1.2$ . To identify the shorter period features in the data we obtain residuals from the best-fit model values. The figure 1c and 1d panels show the nocturnal variability of the residual intensity and temperature respectively. The best-fit model reveals the presence of  $\sim 4.2 \pm 0.2$  and  $3.0 \pm 0.8$  hr wave in the temperature and intensity residuals, respectively. Once again we treat these as the same wave for the reason explained above. The best-fit analysis shows the

amplitudes of this wave to be  $\sim 1.019\%$  and  $3.75\%$  arbitrary units in the temperature and intensity data, respectively. Hence, the  $|\eta|$  value for short period waves is estimated to be  $3.68 \pm 0.9$ . In general we note that in worst case, the maximum error in  $|\eta|$  values are  $<25\%$ . The phase difference between the intensity and temperature waves is obtained with the help of best-fit parameters, which were also verified with a cross correlation analysis. The phase of the principal waves (maxima) (period  $\sim 8.2$  hr) was  $\sim 24.88$  hr in the temperature data and  $24.4$  hr in the intensity data, which results in the phase difference of  $\sim 0.48$  hr, i.e.,  $\Phi$  values of  $-21.07 \pm 12^\circ$ . Similarly, for the shorter period (period  $\sim 4.2$  hr) the  $\Phi$  values are estimated to be  $-114.3 \pm 20^\circ$ . We can also estimate the vertical wavelength with the help of Krassovsky's parameter following the approach elaborated by Tarasick & Hines (1990).

$$\lambda_z = \frac{2\pi\gamma H}{(\gamma - 1)|\eta| \sin(\phi)} \quad (2)$$

where  $\gamma = C_p / C_v = 1.4$  is the ratio of specific heats, and  $H = 6$  km is the scale height. This formula is valid for zenith observations and for plane waves. It is not valid for the evanescent waves. Equation (2), negative vertical wavelength corresponds to downward phase propagation (i.e., upward energy propagation), and that means that temperature oscillations precede the intensity oscillations in phase (e.g., Takahashi, et al. 1990). Using the above relation we find that vertical wavelength for the two cases discussed above are  $\sim -51.5 \pm 15$  and  $-39.3 \pm 40$  km for the long period and the short period waves, respectively. Note that the long period wave estimates may be biased when the data length is comparable to that of the wave period and therefore in our study we have considered only those waves whose periods are substantially less than the length of the available data.

The above analysis was carried out on nighttime events recorded during 2010 and 2011 when the prominent wave features were visible. During the 2010 period, the principal nocturnal waves in the data show the wave periods vary from 5.2 to 10.8 hr with corresponding temperature amplitudes ranging from 2 to 13.8 K. Similarly for 2011, wave periods vary between 5.2 and 8.4 hr with corresponding temperature amplitudes lying between 1.1 K and 15.7 K. However, the intensity amplitudes of the principal waves vary from 7.9% to 49.9 % and 5% to 90% for 2010 and 2011, respectively. We note that the estimated  $|\eta|$  values were found to range from 2.1 - 10.5 for the principal wave. In the case of the short period waves, the periods ranged from 1.5 to 4.4 hr (for 2010) and 2.8 to 4.4 hr (for 2011) with corresponding temperature amplitudes ranging from 0.68 K to 12.2 K and 0.4 K to 14.2 K. The corresponding intensity amplitudes fall in range between  $\sim 1.54\%$  to 46.8% and 1.32% to 46.8% for 2010 and 2011, respectively. The phase ( $\Phi$ ) values also exhibit large variability for long (short) period waves, range in between  $-27^\circ$  and  $-167^\circ$  ( $-27^\circ$  and  $-150^\circ$ ) for 2010 and  $-8.1^\circ$  and  $-65.2^\circ$  ( $-39.1^\circ$  and  $-122.6^\circ$ ) for 2011. For 2010 the deduced vertical wavelengths are found to vary from  $-32.2$  km to  $-140$  km and  $-24$  km to  $-88$  km for the long and short period waves, respectively. Similarly, for 2011 the deduced vertical wavelengths are found to vary from  $-40$  km to  $-102$  km, and  $-26$  km to  $-92.4$  km for the long and short period waves, respectively.

In Figure 2a we plot our results for  $|\eta|$  (hereafter  $\eta$ ) with pink half-filled squares indicating the estimates for the year 2010 and olive half-filled squares for the year 2011. We plot  $\Phi$  in Figure 2b using the same symbols as used in Figure 2a. For a comparison, we also show the values of  $\eta$  and  $\Phi$  of the results from other investigations are shown (Viereck and Deehr 1989; Takahashi et al., 1992; Oznovich et al., 1995, 1997; Drob 1996; Reisin and Scheer 1996; Taylor et al., 2001; Lopez-Gonzalez et al., 2005). Also shown in the figure are the model estimates of

Schubert et al. (1991), Tarasick and Shepherd (1992a, b), Walterscheid and Schubert (1995). We  
 also plot observed  $\eta$  and  $\Phi$  values against their observed period in figure (2a1 and 2b1). In  
 general, we note that the parameter  $\eta$  increases with wave period. It is evident that the observed  
 $\eta$  and  $\Phi$  values in our study show a large spread in their distribution as compared to the model  
 values. A similar spread in the distribution of observed values of  $\eta$  (Figure 2a) from 1.03 to 7.85  
 has also been observed by other investigators (e.g., Takahashi et al., 1992). It may be noted that  
 the values of  $\eta$  for the OH data in our study lie somewhere between the model estimates and the  
 values observed by other investigators. Also noteworthy in this figure is that our  $\eta$  values are  
 closer to the model values reported by Tarasick and Shepherd (1992a) for the waves with  
 horizontal wavelength 500 km. The observed phase ' $\Phi$ ' values, on the other hand show  
 significantly larger deviations from this model for 2010, while for 2011 agreement seems to be  
 better. We note that our measurements of  $\Phi$  matches somewhat with those reported by Viereck  
 and Deehr (1989), while large differences with other published results can be easily noted. The  
 variation of  $\Phi$  values with respect to the wave periodicity, obtained in the 2010 year clearly  
 shows that most of the time we observe values to be higher than those obtained by different  
 models.

Of the importance is that Reisin & Scheer (2001) found  $\eta$  values of  $3.47 \pm 0.07$  corresponding to  
 the wave periods between 1000s and 3h. Our observed values of  $\eta$  (arithmetic mean,  $4.4 \pm 1$  for  
 2010 year and  $5.7 \pm 1.7$  for 2011 year) for OH measurements agree well with this report. In  
 another study based on long-term observations with a spectral airglow temperature imager  
 (SATI) from a mid-latitude station, Lopez-Gonzalez et al. (2005) reported a mean value of  $\eta$  of  
 approximately  $\sim 8.6$  for the OH measurements with a larger variability than our observations  
 show. In another report, Guharay et al. (2008), found that for wave periods ranging from 6 hr to

13 hr, values of  $\eta$  between 1.7 to 5.4, while the phase varied from  $-13^\circ$  to  $-90^\circ$ . Similarly, Aushev et al. (2008) presented amplitudes of the Krassovsky parameter for wave periods of 2.2 to 4.7 hr which in range from 2.4 to 3.6 while the phase values in between  $-63^\circ$  to  $-121^\circ$ . It is noteworthy that our derived values broadly agree with Guharay et al. (2008, 2009), Reisin and Scheer (2001, 2004) and Viereck and Deehr (1989) while they are somewhat different from the values reported by Lopez-Gonzalez et al. (2005) which may be due to the fact that their observations corresponded to higher latitude than ours. It also remains to be seen that when mesopause altitude itself changes from low to high latitudes how would that reflects in the Krassovsky parameters.

The results of ( $\eta$  and  $\Phi$ ) shown in Figure 2 emphasize that there are significant differences in the Krassovsky parameters derived from one study to another. This we suspect to be caused by the variations in the altitudinal profile of oxygen and its effect on the  $\eta$  through the complex OH chemistry (Walterscheid et al., 1994). Another possibility over low latitudes was discussed by Makhlouf et al. (1995) who suggested the quenching caused by the perturbed molecules during their transitions from several vibrational levels. Winds also affect the OH response to gravity waves and therefore they will also contribute to the spread of values seen between the various observation studies (e.g., Sonnemann G. and M. Grygalashvyly, 2003 ).

Note that our observations as well as simulations show the phase  $\Phi$  for OH to be a negative value indicating upward propagating waves (see Tarasick and Shepherd, 1992a, b). In general we note that our  $\Phi$  values, although on some occasions are closer to Viereck and Deehr (1989) observations, show deviations from other investigators and are larger than the model values on most occasions. Differences in theory and observation may be due to the horizontal wavelength assumed in the model and or the Prandtl number (ratio of kinematic viscosity to

277 thermal diffusivity) assumed. The Prandtl number is important in theoretical calculations and  
 278 modeling, especially when in terms of dissipating waves owing to molecular viscosity and  
 279 thermal diffusivity while they propagate in the atmosphere (Hickey 1988). An error in the  
 280 Prandtl number assumption will affect the derived wave parameters ( $\lambda_z$ ,  $\eta$  etc.), which may in-  
 281 turn result in misleading results. In this regard, Makhlof et al. (1995) studied the variations in  
 282 the  $\eta$  values by modifying the model proposed by Hines and using a photochemical dynamical  
 283 model; however, they were still unable to explain the appearance of the negative phases  
 284 appropriately. Hines and Tarasick (1987) found a wide range of  $\eta$  variability, a result supported  
 285 by our measurements. Further, Hines and Tarasick (1997) subsequently discussed the necessary  
 286 correction for thin and thick layer approximations for the calculation of  $\eta$  from airglow  
 287 emissions due to gravity waves interaction. They also pointed out that OH emission intensity,  
 288 which affects the derived  $\eta$  values, does not depend on the oxygen profile and other minor  
 289 species, which contradicts the theory of Walterscheid et al. (1994), Schubert et al. (1991). The  
 290 calculated vertical wavelengths (VW) for all the nights of the observation are shown in Figure 2c  
 291 as pink half filled squares indicating the estimates for the year 2010 and olive half filled squares  
 292 for the year 2011. Large differences exist from one night to another. The VW has a large  
 293 variability ranging from  $-41$  km to  $-102$  km (2010) and  $-36.2$  km to  $-140$  km (2011) for long  
 294 period waves, and,  $-26$  to  $-92.4$  and  $-24$  to  $-88$  km for short period waves period of 2010 and  
 295 2011 years, respectively. In 2010 (and 2011) years, the mean VW values for long and short  
 296 period waves are calculated to be  $-60.2 \pm 20$  km ( $-77.2 \pm 40$  km) and  $-42.8 \pm 15$  km ( $-59.2 \pm 30$   
 297 km), respectively. Further, unlike the clear dependency on the wave period noted in the  
 298 Krassovsky parameters ( $\eta$  and  $\Phi$ ) no clear trend is noted in the calculated VW. We also plot the  
 299 values reported by Reisin and Scheer (1996) and Lopez-Gonzalez et al. (2005) for a comparison.

It is noteworthy that for all the days the VW for the long period wave are higher than the VW of short period waves. We also observed that VW values calculated for 2011 year are larger than 2010 year calculated values. We note that the values reported by Reisin and Scheer (1996) are approximately  $-30$  km with about 40 km variability. Our values are in good agreement with them. However, Lopez-Gonzalez et al. (2005) observed VW values to be approximately  $-10$  km deduced from their OH observations, which do not agree with our values. Further, Ghodpage et al. (2012) analyzed the long-term nocturnal data of 2004-2007 and also observed that the VW lies between 28.6 and 163 km. Recently, Ghodpage et al. (2013) studied the simultaneous mesospheric gravity wave measurements in the OH emission from Gadanki and Kolhapur, inferring mean VWs varying from  $-26$  to  $-60$  km for the Kolhapur observations. Takahashi et al. (1990) reported vertical wavelengths varying from 20 to 80 km, which is in agreement with our values.

#### **4. Comparison with the Full Wave Model Results**

Wave simulations were performed using the Full Wave Model (FWM) for which the representative inputs were taken for the duration of observations reported in section 3. The observations were conducted over an approximate one month period spanning February 8<sup>th</sup> and March 13<sup>th</sup>, and accordingly we used the middle date of this observation period (February 25<sup>th</sup>) in the MSIS model to represent the mean state. The latitude used was  $16.8^\circ$  N, and the local time was midnight. Because the speed and direction of wave propagation were not determined from the observations, several simulations were performed for each wave period in which the direction of propagation (eastward, northward and westward propagation) and the phase speed (50 m/s, 100 m/s and 150 m/s) were varied. Note that the mean winds (not shown) in these simulations

were derived from the Horizontal Wind Model (HWM) using the same input parameters as used for the MSIS model. The derived meridional winds (not shown) are far smaller than the zonal winds for the conditions considered here, and so while results for eastward and westward propagation differed quite markedly, those for northward and southward propagation did not. Hence we considered only a single direction (northward) for meridional propagation.

We also performed a tidal simulation using an equivalent gravity wave model (Lindzen 1970; Richmond 1975), as implemented in an earlier study (Walterscheid and Hickey 2001). The horizontal wavelength and Coriolis parameter are adjusted to give maximal correspondence with a given tidal mode. Here, we performed calculations for the terdiurnal (3,3), (3,4), (3,5) and (3,6) modes using parameters provided by Richmond (1975). The simplifications inherent in this approach are discussed by Walterscheid and Hickey (2001).

Comparisons between the full wave model results for  $\eta$ ,  $\Phi$  and  $\lambda_z$  and the values inferred from the observations are shown in figure 3a, 3b and 3c, respectively. In figure 3a we compare the observed values of  $\eta$  for 2010 and 2011. The observed values of  $\eta$  are represented as pink and olive lower half-filled squares for 2010 and 2011, respectively. In figure 3a we note that at few of the longer wave periods, the observed values of  $\eta$  are in good agreement with the full wave model results. For short period waves the values of  $\eta$  inferred from the observations appear to be bounded by the model values for waves with horizontal phase velocities are 50 and 100 m/s, respectively. For example, for 3.6 hr wave periods, the average of the values of  $\eta$  inferred from the observations is 3.7, while the full wave model values lie between about 0.5 (for the 100 m/s wave) and 7 (for the 50 m/s, eastward propagating wave). For the 8 hr wave periods, the average of the values of  $\eta$  inferred from the observations is 5.7, which is bounded by the full



345 wave model estimates for waves having a horizontal phase velocity of 50 m/s and different  
346 propagation directions.

347 Overall, we note that the comparison between the observed  $\eta$  values and the modeled  
348 values can be explained by gravity waves whose horizontal phase velocities range from 50 m/s to  
349 100 m/s. In this regard, an earlier investigation by Sikha et al. (2010) observed gravity wave  
350 horizontal phase speeds (for periods 5 min to 17 min) varying between 10 m/s and 48 m/s. The  
351 propagation directions were reported to be preferentially towards the north. More recently, Taori  
352 et al. (2013) studied mesospheric gravity wave activity in the OH and OI 558 nm emissions from  
353 Gadanki. They observed that the gravity waves were moving in the north–west direction. The  
354 average phase velocity of the ripple-type waves was found to be 23.5 m/s. The other, band-type  
355 waves, with horizontal scales of about 40 km, were found to be propagating from south to north  
356 with an estimated phase speed of 90 m/s.

357 The vertical wavelengths ( $\lambda_z$ ) calculated using the observed values of  $\eta$  and  $\Phi$  differ  
358 significantly from the full wave model estimate for waves with phase velocities below 100 m/s.  
359 More typically, a comparison between those values inferred from the observations and those  
360 derived from the model tend to agree for phase velocities in the 100 - 150 m/s range. However, it  
361 should be noted that vertical wavelengths inferred from the observations are based on the use of  
362 the inferred Krassovsky's ratio,  $\eta$ , in Eq. (2). Note that the errors in the determination of the  
363 phase ( $\Phi$ ) of  $\eta$  may lead to significant errors (proportional to  $\cot\Phi$ ) in the determination of  $\lambda_z$ ,  
364 especially as  $\Phi$  approaches  $\pm 180^\circ$ .

365 The differences noted in the observed and modeled estimates of Krassovsky ratio  
366 magnitudes  $\eta$  and phase ( $\Phi$ ) may be associated with the limitation arising due to dynamics as  
367 well as the measurements. In terms of measurements limitation, the parameters achieved with the

best fit method may have leaked contribution from other wave components, which may be dynamically varying within a wave period. In terms of dynamics, that full wave model uses climatological density (both major gas and minor airglow-related species) and wind profiles, which will introduce uncertainties. This point has been previously elaborated by Walterscheid et al. (1994) with respect to the effect of a change in the [O] profile on the OH response to wave motions.

It is interesting to note that the arithmetic mean values of  $|\eta|$  for the years 2010 and 2011 were 4.4 and 5.7 respectively. When we look at each  $|\eta|$  value from one wave period range to other, the difference is found to be more than 30% which is well above the maximum errors in the estimation. One may further argue that this difference may not be significant. For this, we looked at the mode of the values for periods ranges 1-4 hr, 4-6 hr, 6-8 hr and 8-10 hr. We found that in each case in the year 2011 mode values are larger than the year 2010. The differences noted in the magnitude of the observed Krassovsky ratio  $\eta$  between 2010 and 2011 may be associated with variations in the height and shape of the undisturbed OH emission profile. We use the SABER data to investigate this aspect. To check whether there was a difference in the OH emission layer structure, we selected the nighttime OH emission profile for a grid encompassing 10°N to 20°N latitudes and 70°E to 90°E latitudes during February, March and April months of the years 2010 and 2011. We have selected the February to March period because the optical airglow data used in this study was acquired primarily during these months. The monthly mean values of OH emission rates are shown in Figure 4. The solid curves correspond to 2010 data while the dashed curves correspond to 2011 data. We note that the peaks of OH emission layer during February, March and April of 2010 occurred at 84.2 km, 82.8 km and 85.1 km altitude, respectively, while the corresponding peaks for 2011 were found to occur

391 at 85.8 km, 85.6 km and 85.2 km altitude. This suggests that the peak of the emission layer  
 392 occurred at a somewhat lower altitude in 2010 compared to 2011. Also, the emission rates during  
 393 February and March were found to be higher in 2010. It is important to note that in an earlier  
 394 study, Ghodpage et al. (2013) compared the Krassovsky ratios at two different latitudes, Gadanki  
 395 (13.5 N, 79.2E) and Kolhapur (16.8°N and 74.2°E) and noted a lower OH emission layer peak  
 396 over Kolhapur and also larger estimated  $\eta$  values over Kolhapur. In the present case, instead of  
 397 the location, it is the difference in the measurement year where the peak emission altitudes of the  
 398 OH emission layer are somewhat different. As the peak emission layer arise due to the chemical  
 399 reactions involving odd oxygen, it is proposed that chemical composition was different from the  
 400 year 2010 to the year 2011. Therefore, modified OH emission rates may be responsible for the  
 401 observed differences in the Krassovsky parameters. A further question that arise here is why the  
 402 peaks should be different from one year to the other. As these months are pre-monsoon, when a  
 403 large scale oscillation namely, El Niño/Southern Oscillation (ENSO) sweeps through the south  
 404 Asian continent, we looked at the ENSO strength based on the Multivariate ENSO Index (MEI).  
 405 This index is shown in table 1, where it is noteworthy that the MEI index for 2010 (January to  
 406 May) is of opposite sign to that for the corresponding months in 2011. We postulate that these  
 407 large scale processes have a profound impact on the observed wave energetics and dynamics at  
 408 mesospheric altitudes. Large scale processes induced the wave oscillations associated with the  
 409 ENSO. The ENSO generates a spectrum of waves which are of planetary scales. These are  
 410 expected to generate a secular variation in temperature and density structure throughout the  
 411 atmosphere. A difference in ENSO suggests that these forcing are different in the two years  
 412 (2010 and 2011). At present, we do not know through which process the ENSO may have

implications in the observed wave characteristics. However, we believe that further investigation is required in order to confirm whether or not any such associations really do exist.

## **5. Conclusion:**

We report the Krassovsky parameters for the observed gravity waves from Kolhapur (16.8°N and 74.2°E) and their comparison with the full wave model.

- 1) The observed values of Krassovsky parameters in our study show a large spread in their distribution as compared to the model values (shown in Figure 2a). A similar spread in the distribution has also been reported by other investigators. We have also observed magnitude of  $\eta$  values is larger in the year 2011 than 2010.
- 2) The values of  $\eta$  for the OH data in our study lie between the model estimates and the values reported in other published results. Whereas the phase values are more than the model values on most occasions. We note that our  $\Phi$  measurements match with those reported by Viereck and Deehr (1989), while they show large differences with the values in other reports.
- 3) Observed vertical wavelength (VW) values broadly agree with the range reported by other investigators and are found to vary from  $-26$  to  $-140$  km. We also noted that VW values calculated for 2011 year are larger than 2010 year calculated values. Most of wave propagating upward in direction.
- 4) Comparison of observed  $\eta$  and  $\Phi$  values agree fairly well with the full wave model results for waves with 50 and 100 m/s horizontal phase velocities. Vertical wavelengths tend to agree for waves with 100 and 150 m/s horizontal phase velocities, except for the

longest period waves for which vertical wavelength cannot be reliably inferred from the observations.

The database used in the present study are limited in terms of the length (time and duration) and locations. Based on the above conclusions we emphasize that more rigorous study using coordinated observations and modeling are required to uncover the physics occurring at upper mesosphere.

## **Acknowledgements**

This work is carried out under the research grant funded by Ministry of Science and Technology and Department of Space, Govt. of India. RNG thank the Director, Indian Institute of Geomagnetism (IIG), Navi Mumbai for encouragement to carry out this work. The night airglow observations at Kolhapur were carried out under the scientific collaboration program (MoU) between IIG, Navi Mumbai and Shivaji University, Kolhapur. MPH acknowledges the support of NSF grant AGS-1001074.

## **6. References**

- Aushev, V. M., Lyahov, V. V., Lopez-Gonzalez, M. J., Shepherd, M. G., and Dryna, E. A.: Solar eclipse of the 29 March 2006: results of the optical measurements by MORTI over Almaty (43.03°N, 76.58°E), *J. Atmos. Sol. Terr. Phys.*, 70, 1088–1101, 2008.
- Bruce, G. H., Peaceman, D. W., Rachford, Jr., H. H., and Rice, J. D.: Calculations of unsteady-state gas flow through porous media, *Petrol. Trans. AIME*, 198, 79-92, 1953.

457 Bittner, M., Offermann, D., Graef, H. H.: Mesopause temperature variability above a midlatitude  
 458 station in Europe. *Journal of Geophysical Research*, 105(D2): 2045–2058, 2000.

459 Drob, D. P.: Ground-based optical detection of atmospheric waves in the upper mesosphere and  
 460 lower thermosphere, Ph. D. Thesis, University of Michigan, Ann Arbor, MI., 1996.

461 Ghodpage, R. N., Singh, D., Singh, R. P., Mukherjee, G. K., Vohat, P., and Singh, A. K.: Tidal  
 462 and gravity waves study from the airglow measurements at Kolhapur (India), *J. Earth Syst.*  
 463 *Sci.*, 121, 6, 1511–1525, 2012.

464 Ghodpage, R. N., Taori, A., Patil, P. T., and Gurubaran, S.: Simultaneous mesospheric gravity  
 465 wave measurements in OH night airglow emission from Gadanki and Kolhapur – Indian low  
 466 latitudes, *Currents Science*, 104, 1, 98-105, 2013.

467 Ghodpage, R. N., Taori, A., Patil, P. T., Gurubaran, S., Sharma, A. K., Nikte, S., and Nade, D.:  
 468 Airglow Measurements of Gravity Wave Propagation and Damping over Kolhapur (16.8° N,  
 469 74.2° E), *International Journal of Geophysics (IJG)*, Volume 2014,1-9,  
 470 <http://dx.doi.org/10.1155/2014/514937>, 2014.

471 Greet, P. A., French, W. J. R., Burns, G B., Williams, P. F. B., Lowe, R. P., and Finlayson, K. :  
 472 OH (6-2) spectra and rotational temperature measurements at Davis, Antarctica, *Annales*  
 473 *Geophysicae*, 16(1), 77–89, 1998.

474 Guharay, A., Taori, A., Bhattacharjee, B., Pant, P., Pande, P., and Pandey, K.: First ground-  
 475 based mesospheric measurements from central Himalayas, *Current Science*, 97, 664-669,  
 476 2009.

477 Guharay, A., Taori, A., and Taylor, M.: Summer-time nocturnal wave characteristics in  
 478 mesospheric OH and O<sub>2</sub> airglow emissions, *Earth Planets Space*, 60, 973–979, 2008.

479 Hecht, J. H., Walterscheid, R. L., Christensen, A. B. and Pranke, J. B.: Observations of wave-  
 480 driven fluctuations of OH nightglow emission bfrom Sondre Stromfjord, Greenland, *J.*  
 481 *Geophys. Res.*, 92, 6091-6099, 1987.

482 Hedin, A. E.: Extension of the MSIS thermosphere model into the middle and lower atmosphere,  
 483 *J. Geophys. Res.*, 96, 1159 – 1172, 1991.

484 Hickey, M. P., and Yu, Y.: A full-wave investigation of the use of a “cancellation factor” in  
 485 gravity wave-OH airglow interaction studies, *J. Geophys. Res.*, 110, A01301,  
 486 doi:10.1029/2003JA01372, 2005.

487 Hickey, M. P., Huang, T.-Y., and Walterscheid, R.: Gravity wave packet effects on chemical  
 488 exothermic heating in the mesopause region, *J. Geophys. Res.*, 108(A12), 1448,  
 489 doi:10.1029/2002JA009363, 2003.

490 Hickey, M. P., Walterscheid R. L., and Schubert, G.: Gravity wave heating and cooling in  
 491 Jupiter’s thermosphere, *Icarus*, 148, 266-281, 2000.

492 Hickey, M. P., Walterscheid, R. L., Taylor, M. J., Ward, W., Schubert, G., Zhou, Q., Garcia, F.,  
 493 Kelley, M. C., and Shepherd G. G.: Numerical simulations of gravity waves imaged over  
 494 Arecibo during the 10-day January 1993 campaign, *J. Geophys. Res.*, 102, 11,475-11,489,  
 495 1997.

496 Hickey, M.P., Schubert, G., and Walterscheid, R. L.: Gravity wave-driven fluctuations in the O<sub>2</sub>  
 497 atmospheric (0-1) nightglow from an extended, dissipative emission region, J. Geophys.  
 498 Res., 98(13),717-730, 1993.

499 Hickey, M. P.: Effects of eddy viscosity and thermal conduction and coriolis force in the  
 500 dynamics of gravity wave driven fluctuations in the OH nightglow, J. Geophys. Res., 93,  
 501 4077, 1988.

502 Hickey, M. P., Taylor, M. J., Gardner, C. S., and Gibbons, C. R.: Full-wave modeling of small-  
 503 scale gravity waves using Airborne Lidar and Observations of the Hawaiian Airglow  
 504 (ALOHA-93) O(1S) images and coincident Na wind/ temperature lidar measurements, J.  
 505 Geophys. Res. 103, 6439-6453,1998.

506 Hickey, M. P., and Cole, K. D.: A quartic dispersion equation for internal gravity waves in the  
 507 thermosphere, J. Atmos. Terr. Phys., 49, 889-899, 1987.

508 Hines, C. O.: A fundamental theorem of airglow fluctuations induced by gravity waves, J.  
 509 Atmos. Sol. Terr. Phys.,59, 319–326, 1997.

510 Hines, C. O., and Tarasick, D. W.: Layer truncation and the Eulerian/ Lagrangian duality in the  
 511 theory of airglow fluctuations induced by gravity waves, J. Atmos. Sol. Terr. Phys., 59, 327–  
 512 334, 1997.

513 Hines, C. O., and Tarasick, D. W.: On the detection and utilization of gravity waves in airglow  
 514 studies, Planet Space Sci., 35, 851–866, 1987.

515 Krassovsky, V. I.: Infrasonic variation of OH emission in the upper atmosphere, Ann. Geophys.,  
 516 28, 739–746, 1972.



517 Lindzen, R. S.: Internal gravity waves in atmospheres with realistic dissipation and temperature,  
 518 part I: Mathematical development and propagation of waves into the thermosphere, *Geophys.*  
 519 *Fluid Dyn.*, 1, 303-355, 1970.

520 Lindzen, R. S., and Kuo, H. L.: A reliable method for the numerical integration of a large class  
 521 of ordinary and partial differential equations, *Mon. Wea. Rev.*, 97, 732-734, 1969.

522 Liu, A. Z., and Swenson, G. R.: A modeling study of O<sub>2</sub> and OH airglow perturbations induced  
 523 by atmospheric gravity waves, *J. Geophys. Res.*, 108, D4, 4151, doi:10.1029/2002JD002474,  
 524 2003.

525 Lopez-Gonzalez, M. J., Rodriguez, E., Shepherd, G. G., Sargoytchev, S., Shepherd, M. G.,  
 526 Aushev, V. M., Brown, S., Garcia-Comas, M., and Wiens, R. H.: Tidal variations of O<sub>2</sub>  
 527 Atmospheric and OH(6-2) airglow and temperature at mid-latitude from SATI observations,  
 528 *Ann. Geophys.*, 23, 3579–3590, 2005.

529 Makhlouf, U. B., Picard, R. H., and Winick, J. R.: Photochemical-dynamical modeling of the  
 530 measured response of airglow to gravity waves, 1: basic model for OH airglow, *J. Geophys.*  
 531 *Res.*, 100, 11,289–11,311, 1995.

532 Mies, F. H.: Calculated vibrational transitions probabilities of OH ( $X^2\pi$ ). *Journal of Molecular*  
 533 *Spectroscopy*, 53, 150–188, 1974.

534 Meinel, A. B.: OH Emission bands in the spectrum of the night sky I. *Astrophys. J.*, 111, 555 –  
 535 564, 1950.

536 Meriwether, J. W.: High latitude airglow observations of correlated short term fluctuations in the  
 537 hydroxyl Meinel 8-3 band intensity and rotational temperature, *Planet. Space Sci.*, 23, 1211–  
 538 1221, 1975.

539 Oznovich, I., Walterscheid, R. L., Sivjee, G. G., and McEwen, D. J.: On Krassovsky's ratio for  
 540 ter-diurnal hydroxyl oscillations in the winter polar mesopause, *Planet Space Sci.*, 45(3), 385–  
 541 394, 1997.

542 Oznovich, I., McEwen, D. J., and Sivjee, G. G.: Temperature and airglow brightness oscillations  
 543 in the polar mesosphere and lower thermosphere, *Planet Space Sci.*, 43, 1121–1130, 1995.

544 Pragati, R.S., Parihar, N., Ghodpage, R., Mukherjee, G.K.: Characteristics of gravity waves in  
 545 the upper mesosphere region observed by OH airglow imaging, *Current Science* 98, 392–397,  
 546 2010.

547 Reisin, E.R., and Scheer, J.: Vertical propagation of gravity waves determined from zenith  
 548 observations of airglow, *Adv. Space Res.* 27(10), 1743-1748, 2001.

549 Reisin, E. R., and Scheer, J.: Characteristics of atmospheric waves in the tidal period range  
 550 derived from zenith observations of O<sub>2</sub>(0-1) Atmospheric and OH (6-2) airglow at lower mid  
 551 latitudes, *J. Geophys. Res.*, 101, 21,223–21,232, 1996.

552 Richmond, A. D.: Energy relations of atmospheric tides and their significance to approximate  
 553 methods of solution for tides with dissipative forces, *J. Atmos. Sci.*, 32, 980-987, 1975.

554 Schubert, G., Hickey, M. P., and Walterscheid, R. L.: Heating of Jupiter's thermosphere by the  
 555 dissipation of upward propagating acoustic waves, *Icarus*, 163, 398-413, 2003.

556 Schubert, G., Walterscheid, R. L., and Hickey, M. P.: Gravity wave-driven fluctuations in OH  
 557 nightglow from an extended, dissipative emission region, *J. Geophys. Res.*, 96 (A8), 13,869–  
 558 13, 880, 1991.

559 Sivjee, G. G., and Hamwey, R. M.: Temperature and chemistry of the polar mesopause OH.  
 560 *Journal of Geophysical Research*, 92(A5): 4663–4672, 1987.

561 Stubbs, L. C., Boyd, J. S., and Bond, F. R.: Measurement of the OH rotational temperature at  
 562 Mawson, East Antarctica, *Planet. Space Sci.*, 31 (8), 923–932, 1983.

563 Sonnemann, G. and Grygalashvyly, M.: The zonal wind effect on the photochemistry within the  
 564 mesosphere / menopause region, *Adv. Space Res. Vol. 32 ( 5)*, 719-724, 2003.

565 Takahashi, H., Buriti, R. A., Gobbi, D., and Batista, P. P.: Equatorial planetary wave signatures  
 566 observed in mesospheric airglow emissions, *J. Atmos. Sol. Terr. Phys.*, 64, 1263–1272, 2002.

567 Takahashi, H., Sahai, Y., Batista, P. P., and Clemesha, B. R.: Atmospheric gravity wave effect  
 568 on the airglow O<sub>2</sub>(0-1) and OH (9-4) band intensity and temperature variations observed from  
 569 a low latitude station, *Adv. Space Res.*, 12(10), 131–134, 1992.

570 Takahashi, H., Sahai, Y., and Teixeira, N.R.: Airglow intensity and temperature response to  
 571 atmospheric wave propagation in the mesopause region, *Adv. Space Res.* 10, (10)77-(10)81,  
 572 1990.

573 Takahashi, H, Batista, P. P, Buriti, R. A, Gobbi, D, Nakamura, T, Tsunda, T and Fukao, S.:  
 574 Simultaneous measurements of airglow OH emission and meteor wind by a scanning photometer  
 575 and the MU radar. *Journal of Atmospheric and Solar-Terrestrial Physics*, 60(17): 1649–1668,  
 576 1998.

577 Tarasick, D. W. and Hines, C. O.: The observable effects of gravity waves in airglow emission,  
 578 Planet. Space Sci., 38, 1105–1119, 1990.

579 Taylor, M. J., Gardner, L. C., and Pendleton, Jr. W. R.: Long-period wave signatures in  
 580 mesospheric OH Meinel (6,2) band intensity and rotational temperature at mid-latitudes, Adv.  
 581 Space Res., 27(6–7), 1171– 1179, 2001.

582 Taylor, M. J., Turnbull, D. N., and Lowe, R. P.: Coincident imaging and spectrometric  
 583 observations of zenith OH nightglow structure, Geophys. Res. Lett., 18, 1349–1352, 1991.

584 Taori, A., and Taylor, M. J.: Characteristics of wave induced oscillations in mesospheric O<sub>2</sub>  
 585 emission intensity and temperatures, Geophys. Res. Lett., 33, L01813,  
 586 doi:10.1029/2005GL024442, 2006.

587 Taori, A., Taylor, M. J., and Franke, S.: Terdiurnal wave signatures in the upper mesospheric  
 588 temperature and their association with the wind fields at low latitudes (20°N), J. Geophys.  
 589 Res., 110, D09S06, doi: 10.1029/2004JD004564, 2005.

590 Taori, A., Jayaraman, A., and Kamalakar, V.: Imaging of mesosphere–thermosphere airglow  
 591 emissions over Gadanki (13.5°N, 79.2° E)-first results, J. Atmos. Sol. Terr. Phys. 93, 21–28,  
 592 <http://dx.doi.org/10.1016/j.jastp.2012.11.007>, 2013.

593 Tarasick, D. W., and Shepherd, G. G.: Effects of gravity waves on complex airglow chemistries:  
 594 1. O<sub>2</sub>(b<sup>1</sup>Σ<sup>+</sup><sub>g</sub>) emission, J. Geophys. Res., 97, 3185–3193, 1992a.

595 Tarasick, D. W., and Shepherd, G. G.: Effects of gravity waves on complex airglow chemistries:  
 596 2. OH emission, J. Geophys. Res., 97, 3195–3208, 1992b.

597 Vargas, F., Swenson, G., Liu, A., and Gobbi, D.: O(<sup>1</sup>S), OH, and O<sub>2</sub>(b) airglow layer  
 598 perturbations due to AGWs and their implied effects on the atmosphere, J. Geophys. Res, 112,  
 599 D14102, doi:10.1029/2006JD007642, 2007.

600 Viereck, R. A., and Deehr, C. S.: On the interaction between gravity waves and the OH Meinel  
 601 (6-2) and O<sub>2</sub> Atmospheric (0-1) bands in the polar night airglow, J. Geophys. Res., 94, 5397–  
 602 5404, 1989.

603 Walterscheid, R. L., and Schubert, G.: Dynamical-chemical model of fluctuations in the OH  
 604 airglow driven by migrating tides, stationary tides, and planetary waves, J. Geophys. Res.,  
 605 100, 17,443–17,449, 1995.

606 Walterscheid, R. L., and Hickey, M. P.: One-gas models with height-dependent mean molecular  
 607 weight: Effects on gravity wave propagation, J. Geophys. Res., 106, 28,831-28,839, 2001.

608 Walterscheid, R. L., Schubert, G., and Hickey, M. P.: A Comparison of Theories for Gravity  
 609 Wave Induced Fluctuations in Airglow Emissions, J. Geophys. Res., 99, 3935, 1994.

610 Walterscheid, R. L., Schubert, G., and Hickey, M. P.: Comparison of theories for gravity wave  
 611 fluctuations in airglow emissions, J. Geophys. Res., 99, 3935–3944, 1994.

612 Walterscheid, R. L., Schubert, G., and Straus, J. M.: A dynamical chemical model of wave-  
 613 driven fluctuations in the OH nightglow, J. Geophys. Res., 92, 1241 – 1254, 1987.

614  
 615  
 616

**Figure captions:**

**Figure 1.** Nocturnal variability in the mesospheric OH emissions on 26-27 January 2011. The upper panels represent the mean deviations in (a) intensity and (b) temperature data. Bottom panels represent (c) intensity and (d) temperature residuals. Solid line curves in each plot show the result of simple best-fit cosine model.

**Figure 2 (a)** Distribution of Krassovsky parameter ' $\eta$ ', reported by investigators (list not exhaustive). The x -axis shows the wave periodicity and the y-axis is for amplitude of Krassovsky parameters ( $\eta$ ) The legends in the figure are as following: ( 1 (for 2010 year) & 2 (for 2011 year)- present study ; 3,Schubert et al. 500 km; 4, Schubert et al. 1000 km; 5, Tarasick and Shepherd 500 km; 6,Tarasick and Shepherd 1000 km; 7, Takahashi et al. (1992); 8, Oznovich et al. (1995); 9, Drob et al. (1996); 10, Reisin and Scheer (1996); 11, Taylor et al. (2001); 12, Guharay et al (2008); 13, Walterscheid and Schubert (1995); 14, Lopez-Gonzalez et al. (2005); 15, Oznovich et al. (1997)); 16, Viereck and Deehr (1989).

**Figure 2 (a1)** Observed values of  $\eta$  versus wave period over Kolhapur alone.

**Figure 2 (b)** Distribution of phase values of Krassovsky parameter ' $\Phi$ ', reported by investigators (list not exhaustive) (1 (for year 2010) & 2 (for year 2011)- present study; 3,Schubert et al. 500 km; 4, Schubert et al. 1000 km; 5, Tarasick and Shepherd 500 km; 6, Tarasick and Shepherd 1000 km; 7,Viereck and Deehr (1989); 8, Oznovich et al. (1995); 9, Drob et al. (1996); 10, Reisin and Scheer (1996); 11, Taylor et al. (2001); 12, Guharay et al.(2008); 13, Walterscheid and Schubert (1995); 14, Lopez-Gonzalez et al. (2005); 15, Oznovich et al. (1997); 16,Viereck and Deehr (1989);).

**Figure 2 (b1)** Observed values of  $\Phi$  verses wave period over Kolhapur alone.

**Figure 2(c)** Deduced vertical wavelength (VW) for both the short and long period wave as function of wave periodicity compared to other published results.

**Figure 3(a)** Comparison with  $\eta$  calculated by observation of both year and Full wave model simulation with their respective wave period. Pink and olive lower half filled square shows the 2010 and 2011 year  $\eta$  observations (1 and 2 present study  $\eta$ ; 3, FWM simulation of  $\eta$  for 50 m/s horizontal phase velocity; 4, FWM simulation of  $\eta$  for 100 m/s horizontal phase velocity; 5, FWM simulation of  $\eta$  for 150 m/s horizontal phase velocity).

**Figure 3(b)** Simillar to figure 3(a) but for phase values for both the short and long period wave.

**Figure 3(c)** Simillar to figure 3(a) but for deduced vertical wavelength (VW).

**Figure 4.** The monthly (February, March and April ) mean OH emission rate profiles from SABER for the year 2010 (solid lines) and 2011 (dashed lines).

**Table 1.** Comparisons of deduced wave parameters in 2010 and 2011 years with MEI index and OH altitudes. The observed quantities are mean for their representative wave periods. (JFM-January, February and March months like this)

26 - 27 January 2011; Kolhapur

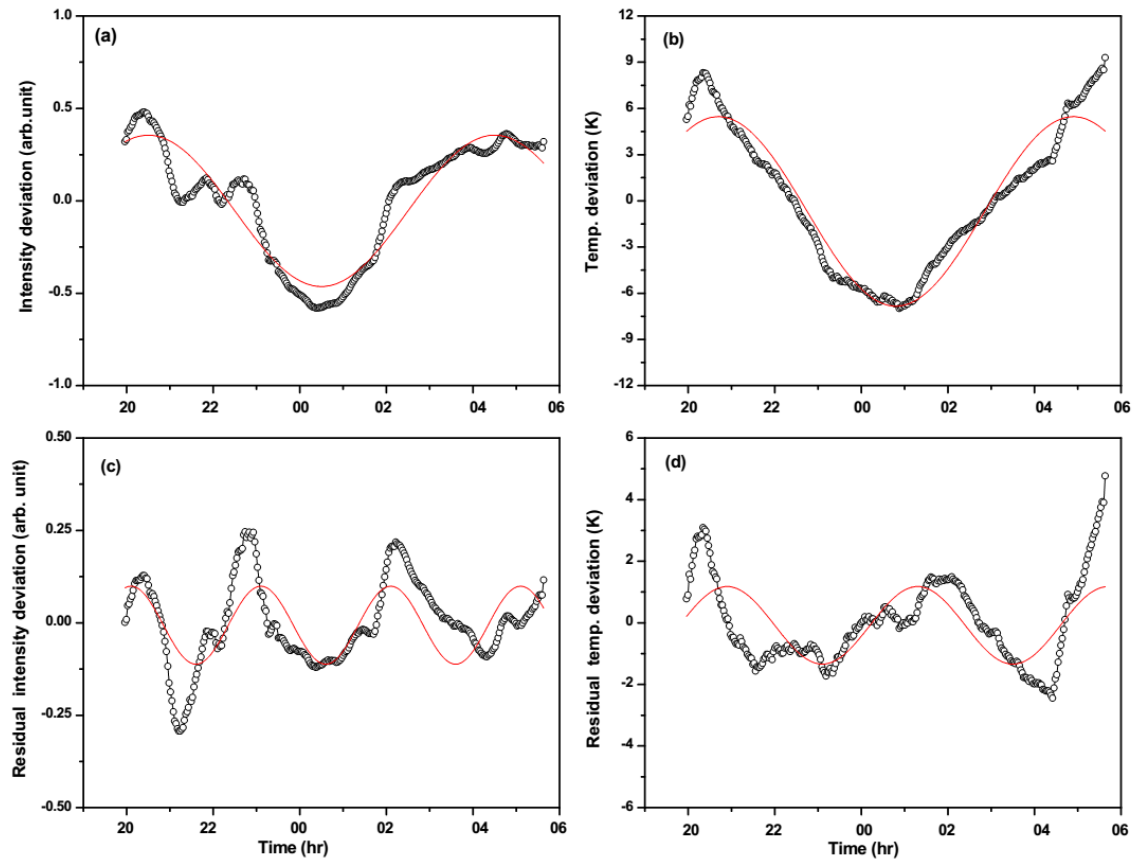


Figure 1.



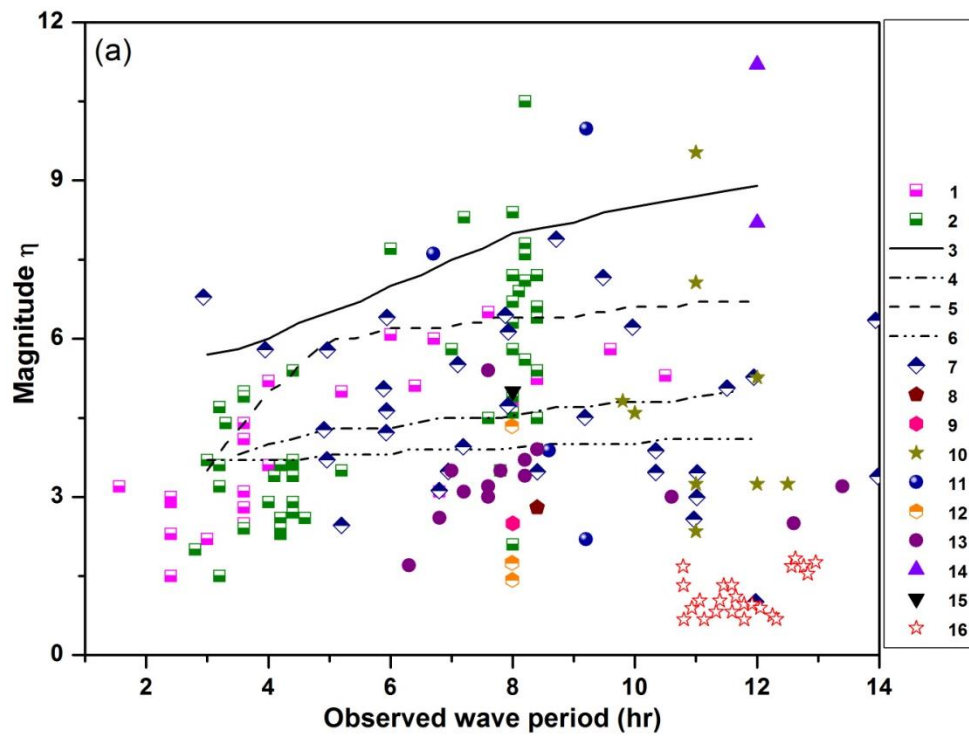


Figure 2(a)

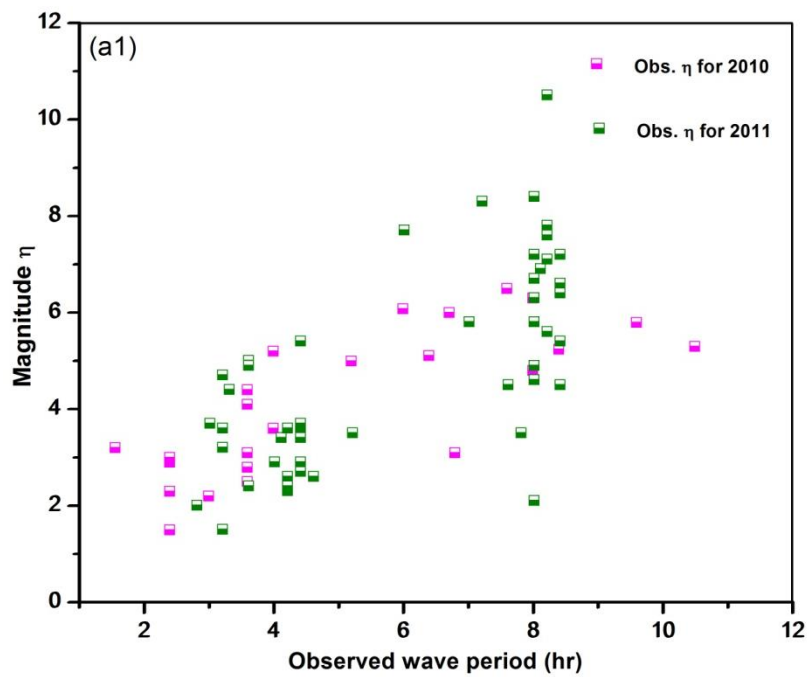
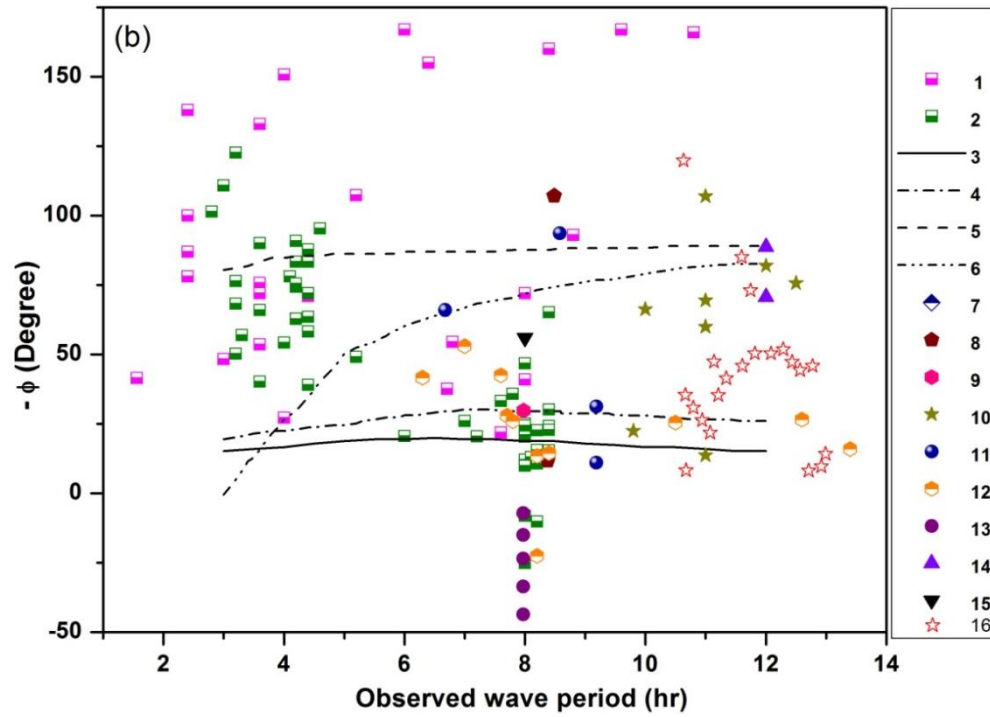
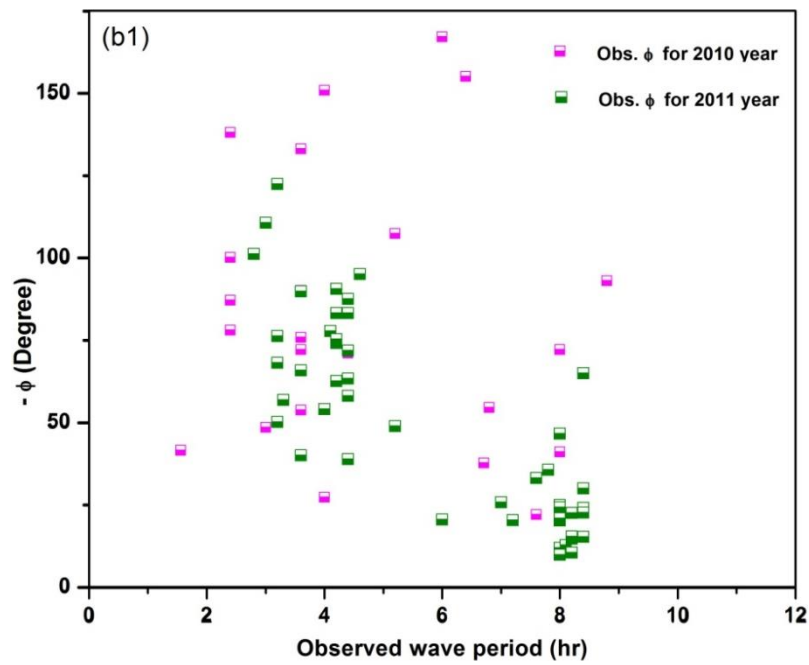


Figure 2(a1)



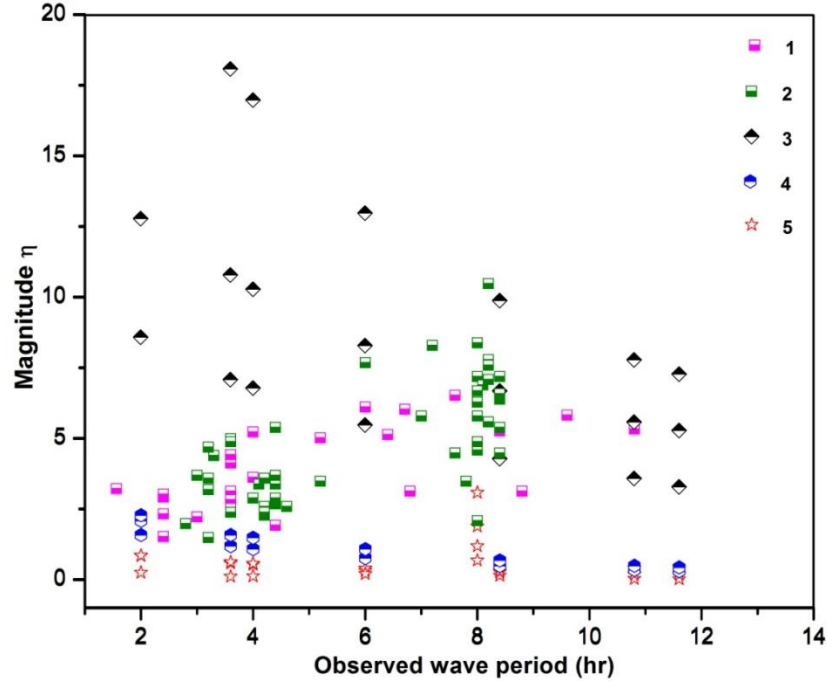
664 Figure 2(b)



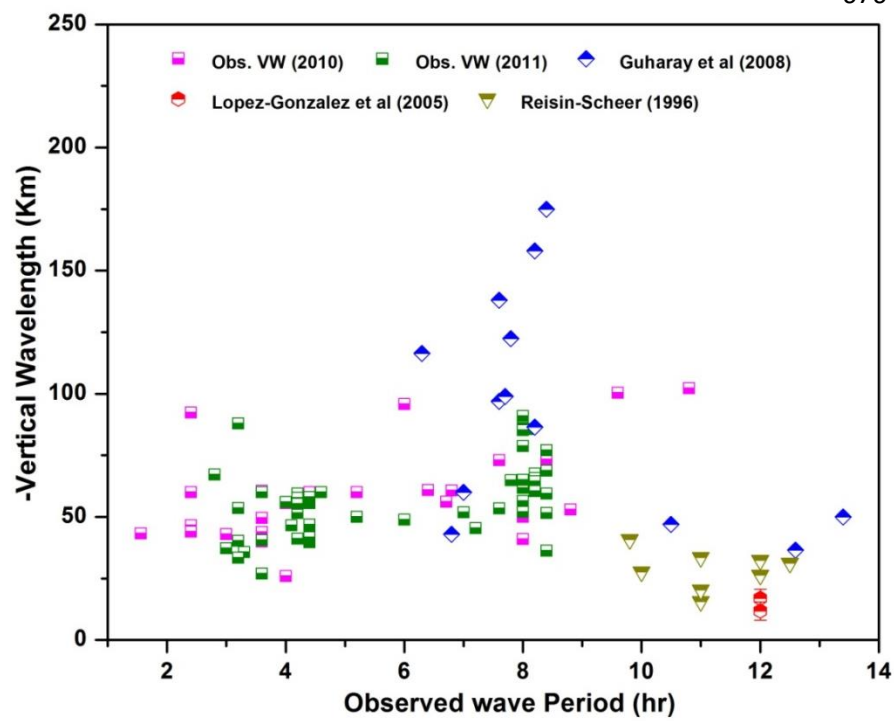
666

667 Figure 2(b1)

668

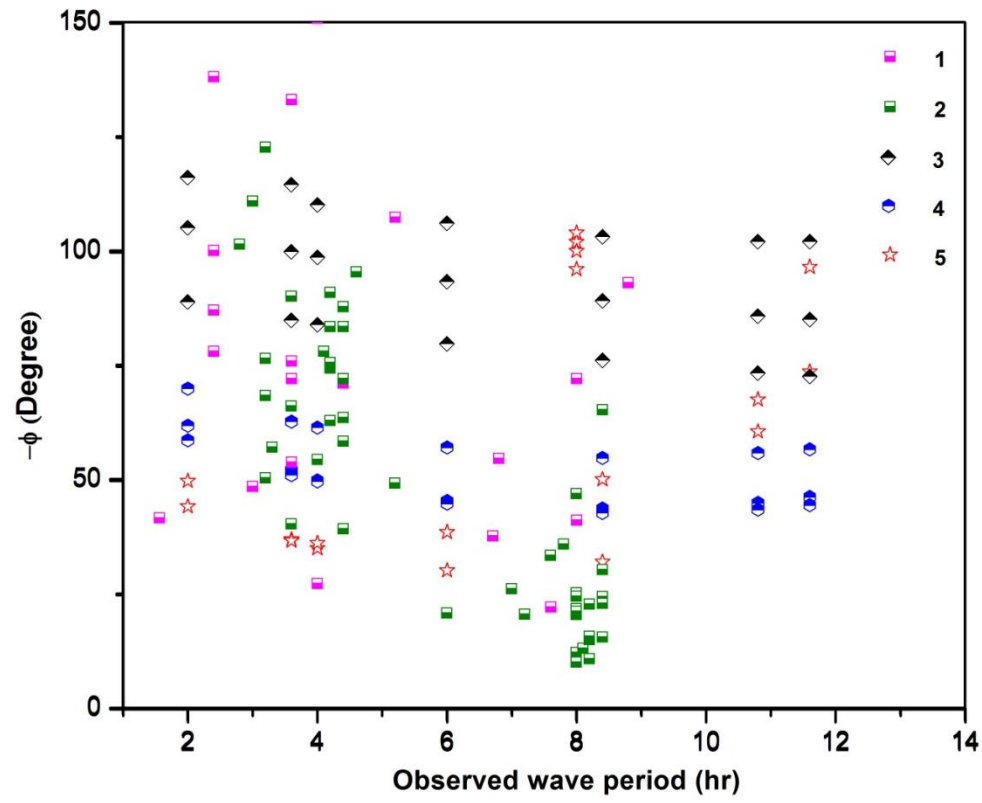


675 Figure 2(c)



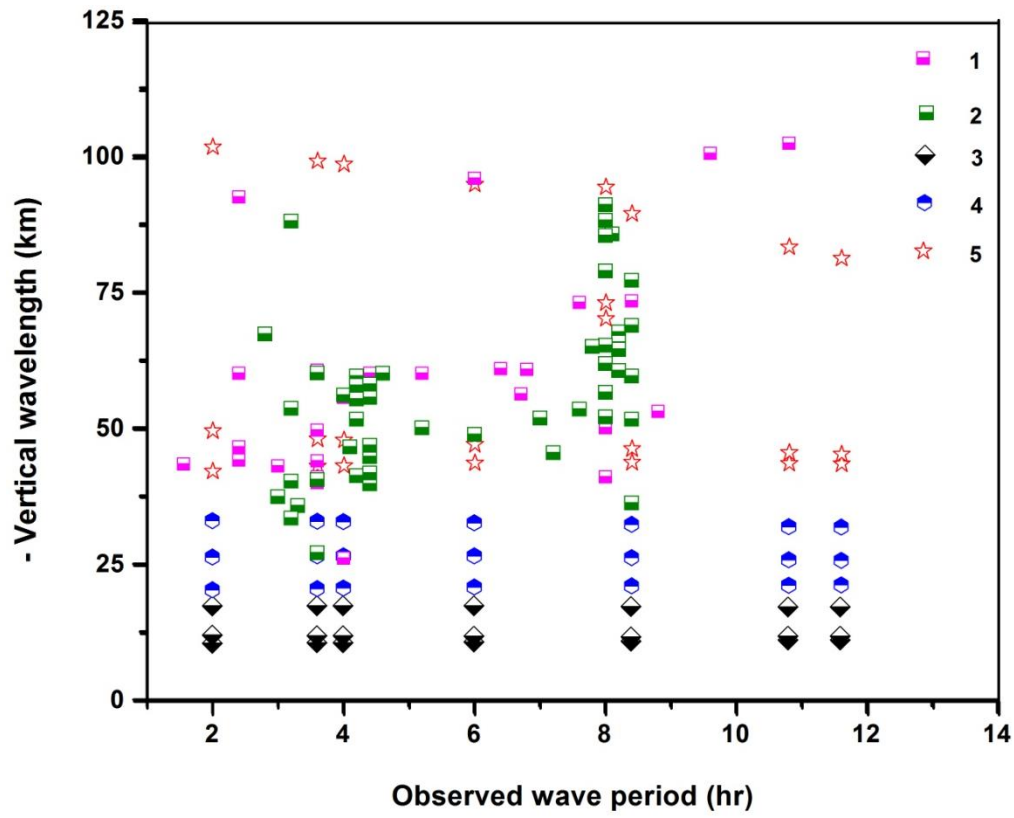
677

678 Figure (3a)



679

680 | Figure 3(b)



681

682 Figure 3 (c)

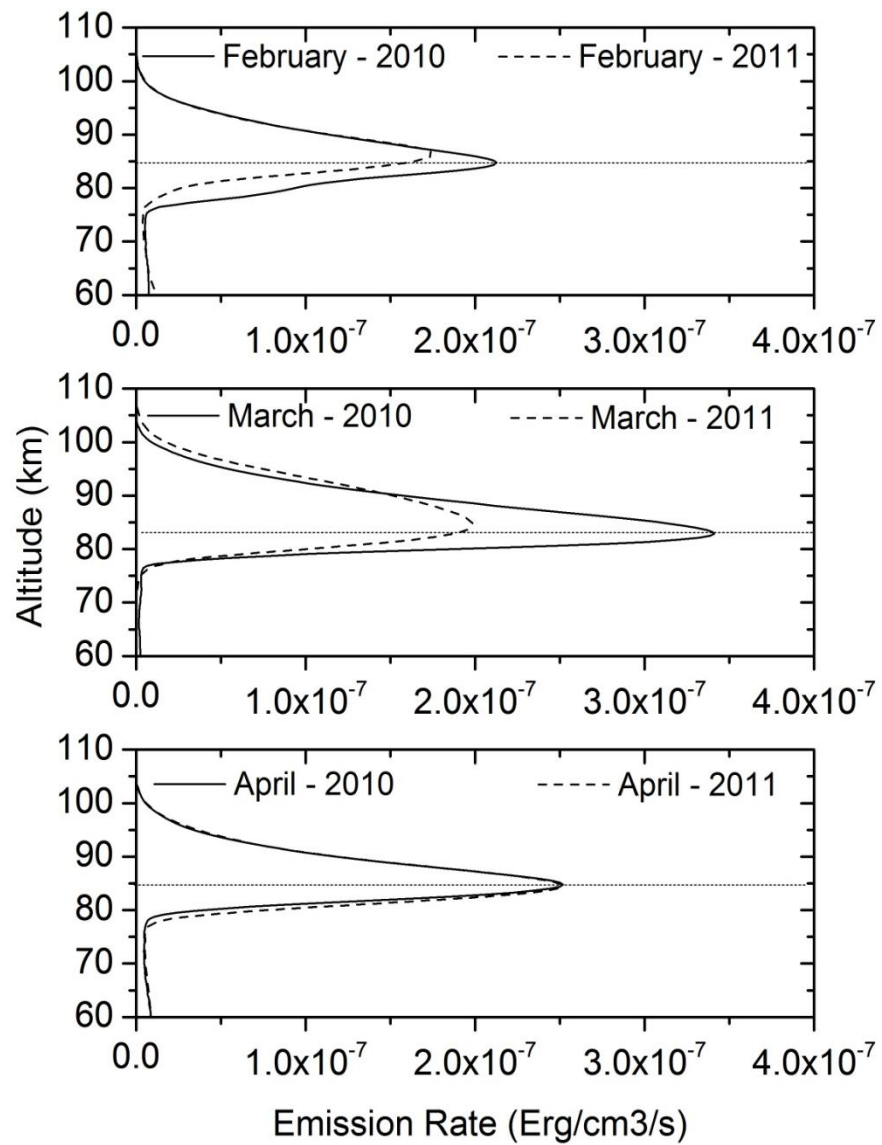


Figure 4.

690 Table 1.

Year	Mean $\eta$ ( $\pm$ Errors)		Mean ( $-\Phi$ ) (Deg.)		Mean ( $-VW$ ) (km)		OH altitude (km)	MEI index				
	Long wave period	Short wave period	Long wave period	Short wave period	Long wave period	Short wave period		JFM	FMA	MAM	SON	OND
2010	4.4 $\pm$ 1	2.3 $\pm 0.9$	90.6 $\pm 40$	70.4 $\pm$ 45	60.2 $\pm 20$	42.8 $\pm 15$	82 km to 85.1 km during February – April	1.1	0.8	0.5	-1.4	-1.3
2011	5.7 $\pm$ 1.7	2.7 $\pm 0.6$	33.8 $\pm 40$	64.4 $\pm$ 40	77.6 $\pm 40$	59.2 $\pm 30$	85.1 km to 86 km during February – April	-1.1	-0.8	-0.6	-0.9	-0.9

691

692